Brune, S., Autin, J. (2013): The rift to break-up evolution of the Gulf of Aden: Insights from 3D numerical lithospheric-scale modelling. - *Tectonophysics*, *607*, 65-79

DOI: 10.1016/j.tecto.2013.06.029

The rift to break-up evolution of the Gulf of Aden: Insights from 3D numerical lithospheric-scale modelling

Sascha Brune
Helmholtz Centre Potsdam, GFZ German Research Centre for Geosciences
Section 2.5, Geodynamic Modelling, Potsdam, Germany
Julia Autin
IPGS - UMR 7516; Université de Strasbourg/EOST, CNRS

Corresponding author: Sascha Brune
Email: brune@gfz-potsdam.de, Tel: +49 331 2881928, Fax: +49 331 288 1938

Abstract

The Gulf of Aden displays an ideal setting to study oblique rifting since numerous structural data are available onshore and offshore. Recent surveys showed that the spatio-temporal evolution of the Gulf of Aden rift system is dominated by three fault orientations: displacement-orthogonal (WSW), rift-parallel (WNW) and a direction that is intermediate between both of them (W). The oldest parts of the rift that are exposed onshore feature displacement-orthogonal and intermediate directions, whereas the subsequently active necking zone involves mainly rift-parallel faults. The final rift phase that is recorded at the distal margin is characterised by displacement-orthogonal and intermediate azimuths. We investigate the Gulf of Aden evolution from rift initiation to break-up by means of 3D numerical experiments on lithospheric scale. We apply the finite element model SLIM3D which includes realistic elasto-visco-plastic rheology and a free surface. Despite recent advances, 3D numerical experiments still require relatively coarse resolution so that individual faults are poorly resolved. We address this issue by proposing a simple post-processing method that uses the surface stress-tensor to evaluate stress regime (extensional, strike-slip, compressional) and preferred fault azimuth. The described method is applicable to any geodynamic model and easy to introduce. Our model reproduces the observed fault pattern of the Gulf of Aden and illustrates how multiple fault directions arise from the interaction of local and far-field tectonic stresses in an evolving rift system. The numerical simulations robustly feature intermediate faults during the initial rift phase, followed by rift-parallel normal faulting at the rift flanks and strike-slip faults in the central part of the rift system. Upon break-up, displacement-orthogonal as well as intermediate faults occur. This study corroborates and extends findings from previous analogue experiments of oblique rifting on lithospheric scale and allows new insights in the timing of fault successions of the Gulf of Aden and continental rifts in general.

1. Introduction

By nature, oblique rifts need to be studied in three dimensions and their understanding still depends on the ability to reproduce 3D processes. The Tertiary Gulf of Aden is an ideal area to study oblique rifting. The direction of extension is N025°E but the rift has a N075°E-trend (Fig. 1), resulting in a moderately oblique rift system. The fault pattern is well expressed on present day conjugate margins. Moreover, the oceanic basin is young (17,6 My) so that the sedimentary cover is thin and the conjugate margins are easily correlated.

The Gulf of Aden rift system formed 34-33 My ago and has been active until continental break-up occurred 20 My ago (Leroy et al. 2012). The Gulf of Aden displays a high segmentation with large fracture zones that delimit three distinct segments (Eastern, Central, and Western Segment, Fig. 1a): The Eastern Gulf of Aden features extremely thin transitional crust at the Ocean-Continent Transition (OCT) (Leroy et al. 2010; Watremez et al. 2011), which most likely exhibits exhumed serpentinised mantle rocks indicating a magma-poor setting (Leroy et al., 2012). In both the Eastern and the Central Gulf of Aden, margins are thought to be magma-poor as no magmatic structures as seaward dipping reflectors were recognised in the OCT (e.g. Bosworth et al., 2005). In the Western Gulf of Aden, the margins displays volcanic characteristics related to the activity of the Afar hot spot.

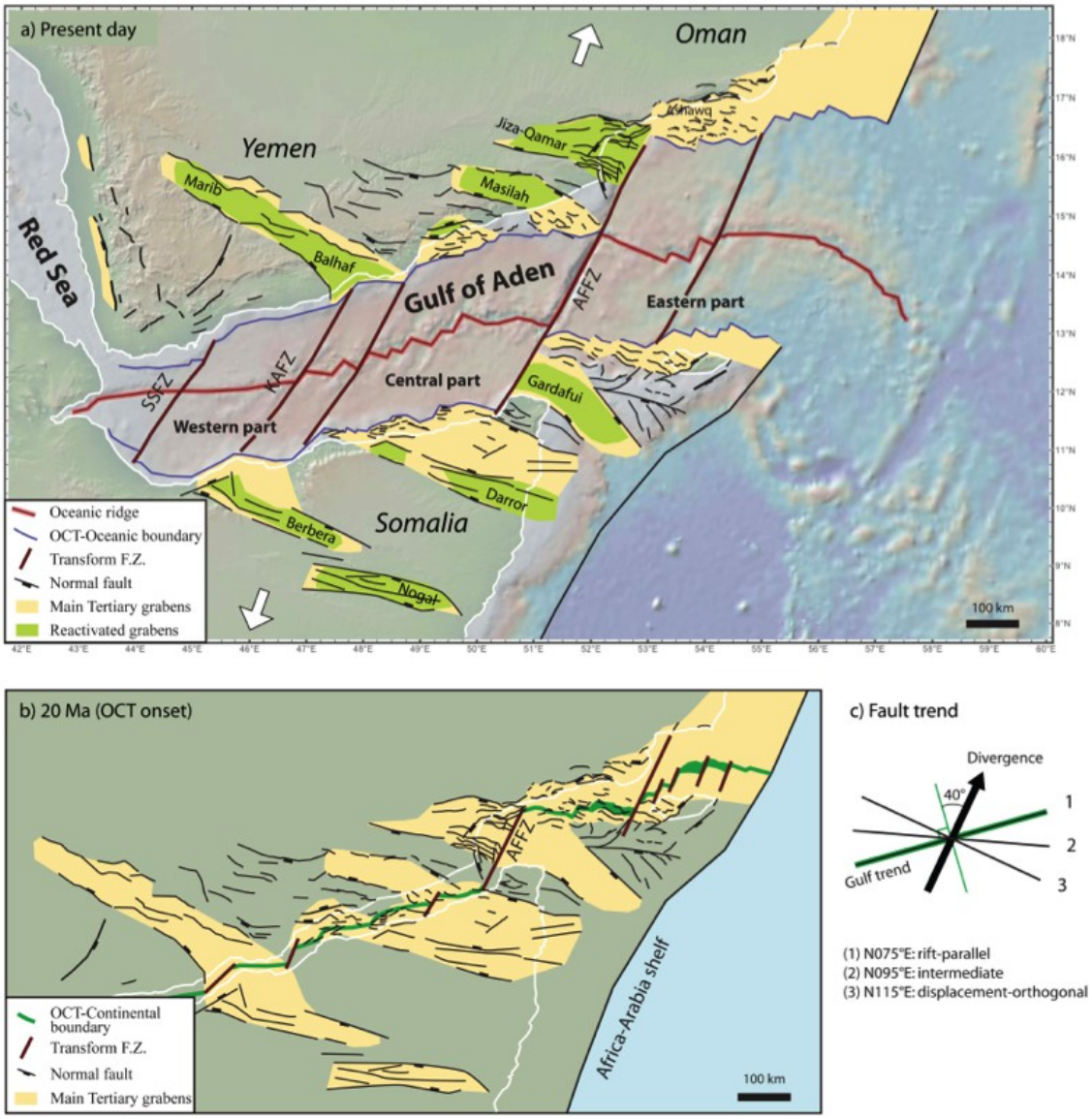

Figure 1: Gulf of Aden overview map. ***(a)*** *Structural map of the Gulf of Aden with the main Tertiary depocentres as well as the Mesozoic inherited basins (after Bellahsen et al., this volume and Leroy et al, 2012). SSFZ: Shukra El Sheik Fracture Zone, KAFZ: Khanshir Al Irquah Fracture Zone, AFFZ: Alula-Fartak Fracture Zone.* ***(b)*** *Reconstruction of the margins at the onset of the ocean-continent transition (OCT) based on Leroy et al., 2012. (c) Major fault trends observed in the Gulf of Aden.*

Previously, the structural pattern of the Gulf of Aden has been elucidated thanks to field and seismic studies that were conducted onshore and offshore Oman (Fournier et al., 2004; d'Acremont et al., 2005; Bellahsen et al., 2006) and in Yemen (Huchon and Khanbari, 2003). They allow to recognise three general fault populations (i) displacement-normal with a fault azimuth of N115°E, (ii) rift-parallel with N075°E and (iii) an orientation that is intermediate in between the two former directions (N095°E). The inversion of fault slip data sets allowed to compute stress tensors corresponding to several local directions of extension (N025°E, N160°E and N-S) in Oman (Lepvrier et al., 2002; Fournier et al., 2004; Bellahsen et al., 2006), in Yemen (Huchon et

al., 1991; Huchon and Khanbari, 2003) and on Socotra Island (Fournier et al., 2007). Offshore, near the OCT, both the faults and basins mainly strike perpendicular to the Gulf of Aden opening direction (d'Acremont et al., 2005). Bellahsen et al. (this volume) observe that the proximal parts of the margins display intermediate and displacement-orthogonal faults, whereas the OCT display rift-parallel or displacement-orthogonal faults and the oceanic ridge is orthogonal to the divergence (Tamsett and Searle, 1988; Dauteuil et al., 2001; Hébert et al., 2001). The overall pattern of deformation in the Gulf of Aden show en-echelon Tertiary sigmoid grabens. This structuration could be linked to Mesozoic inheritance which consists in elongated E-W grabens (Fig. 1b). Previous analogue models of the Arabian plate tend to demonstrate that the obliquity of the Gulf of Aden arises from the interaction between the laterally-evolving subduction of the Tethyan Ocean toward the north and the Afar hot spot in the south-west (Bellahsen et al., 2003).

Fault patterns of oblique rifts have been investigated during the last decades using analogue models on two different levels of complexity: (i) Crustal scale models simplify the rift system to a deforming crust influenced by a basal zone of extension that involves an oblique velocity discontinuity (Withjack and Jamison, 1986; Tron and Brun, 1991; McClay and White, 1995; Clifton et al., 2000; Mart and Dauteuil, 2000; Corti et al., 2001, 2003; Corti, 2004; Sokoutis et al., 2007). The advantage of this setup is that crustal strain patterns can be studied independently of mantle deformation, but this also limits the applicability to the first rift stage where isostatic balancing with the mantle and lithospheric necking can be neglected. Furthermore, the role of the basal discontinuity is overestimated intrinsically. (ii) Analogue experiments on lithospheric scale have been conducted recently and did successfully reproduce lithospheric thinning and its effect on crustal fault patterns (Sokoutis et al., 2007, Agostini et al. 2009, Autin et al. 2010). However, thermal effects or rheological changes occurring during rifting are not modelled in these experiments and their absence remains a significant limitation of such analogue models. They also do not show the progression from oblique rift initiation to plate rupture.

In contrast to analogue models, state-of-the-art geodynamic codes are capable of computing realistic temperature-dependent viscosity as well as complex elasto-visco-plastic rheologies. Many numerical models include these features and have been used to study diverse aspects of rift dynamics in two dimensions (e.g. Zuber and Parmentier, 1986; Braun and Beaumont, 1989; Bassi, 1991; Buck, 1991; Burov and Cloetingh, 1997; Lavier et al., 2000; Behn et al., 2002; van Wijk and Cloetingh 2002; Huismans and Beaumont, 2003; Lavier and Manatschal, 2006; Regenauer-Lieb et al., 2006; Buiter et al. 2008; Huismans and Beaumont, 2011, Rey et al. 2011). Despite these advantages, numerical models of oblique rifting intrinsically require computationally expensive calculations in three dimensions. Addressing only crustal deformation of a rift system strongly limits the computational effort which allows for comparatively higher resolution (Katzman et al. 1995; Allken et al., 2011, 2012), however it is valid only during the initial rift stage, where the influence of a deforming mantle lithosphere can be neglected. This disadvantage is overcome by numerical experiments that involve both crust and mantle lithosphere (Dunbar and Sawyer, 1996; van Wijk and Blackman, 2005; van Wijk, 2005; Le Pourhiet et al. 2012). Nevertheless, these models do not account for weak asthenospheric rheology which becomes influential during late rift stages and continental break-up. Recently, 3D thermo-mechanical rift models featuring crust, lithospheric mantle as well as asthenospheric mantle have been published: Gac and Geoffroy (2009) investigated the influence of weak, melt-related soft points within an extending lithosphere. They show that resultant 3D crustal structures agree well with the tectonic segmentation and zig-zag pattern found at volcanic passive margins. Brune et al. (2012) showed by means of a simple analytical model that oblique rifting is energetically preferred over rift-perpendicular extension, which they corroborated by means of lithospheric-scale numerical experiments. This model has been extended in order to investigate the influence of plume-related lithosphere erosion on the dynamics of continental break-up (Brune et al. 2013).

In this paper, we show that lithospheric-scale numerical experiments are capable to reproduce extensional structures from initial rifting to break-up. We thereby apply elasto-visco-plastic rheology with laboratory-based flow laws for temperature/stress-dependent viscosity. We investigate the fault geometries during oblique rifting based on strain-rate and plastic strain patterns. Moreover, we exploit the fact that numerical models provide direct access to the stress tensor at any numerical element, which allows to infer fine-scale fault patterns. We explicitly compare our experiments to previous analogue modelling results and relate them to present structural knowledge about the Gulf of Aden.

2. Model description

2.1. Numerical model: Setup and Methods

We consider a rectangular Earth segment that consists of a 20 km thick upper crustal layer with a wet quartzite rheology (Gleason and Tullis, 1995), a lower crustal layer of 15 km thickness of granulite properties (Wilks and Carter, 1990), and a 45 km thick layer of strong mantle material with dry olivine rheology (Hirth and Kohlstedt, 2003). We introduce a chemical asthenosphere by applying the flow law of wet (i.e. 500 ppm H/Si) olivine below 90 km depth (Hirth and Kohlstedt, 2003). The thermal lithosphere-asthenosphere boundary (LAB) that is defined here as the 1350 °C isotherm is set to 100 km depth at the start of the model (Fig. 2a,b) The thermal state of the model is initialised as the equilibrium temperature distribution that results from thermal material parameters and the following boundary conditions: the surface temperature is held constant at 0 °C, below 100 km depth the asthenosphere temperature is set to 1350 °C, and lateral boundaries are thermally isolated.. A linear seed is introduced in the model centre by elevating the LAB with an amplitude of 20 km in a region of 20 km width as depicted by the 1350 °C isotherm in Fig. 2a. During subsequent model evolution we fix the bottom boundary temperature to 1350 °C. Our simulation domain measures 249 km times 249 km horizontally and 120 km vertically. We thereby use 275560 cubic elements with a length of 3 km. All rheological and thermal parameters are listed in Table 1. In the following, we refer to this setup as “standard scenario”. Alternative setups where LAB depth and resolution is modified are discussed in Section 3.3.

Parameter	**Upper Crust**	**Lower Crust**	**Strong Mantle**	**Weak Mantle**
Density, ρ (kg m^{-3})	2700	2850	3300	3300
Thermal expansivity, α_T (10^{-5} K^{-1})	2.7	2.7	3.0	3.0
Bulk modulus, K (GPa)	55	63	122	122
Shear modulus, G (GPa)	36	40	74	74
Heat capacity, C_p (J kg^{-1} K^{-1})	1200	1200	1200	1200
Heat conductivity, λ (W K^{-1} m^{-1})	2.5	2.5	3.3	3.3
Radiogenic heat production, A (μW m^{-3})	1.5	0.2	0	0
Initial friction coefficient, μ (-)	0.6	0.6	0.6	0.6
Maximum plastic friction softening*	90 %		none	none
Cohesion, c (MPa)	5.0	5.0	5.0	5.0
Pre-exponential constant for diffusion creep , log(B_{Diff}) (Pa^{-1} s^{-1})	-	-	-8.65	-8,65
Activation energy for diffusion creep, E_{Diff} (kJ / mol)	-	-	375	335
Activation volume for diffusion creep, V_{diff} (cm^{-3} / mol)	-	-	6	4
Pre-exponential constant for dislocation creep , log(B_{Disloc}) (Pa^{-n} s^{-1})	-28.0	-21.05	-15.56	-15.05
Power law exponent for dislocation creep, n	4.0	4.2	3.5	3.5
Activation energy for dislocation creep, E_{Disloc} (kJ / mol)	223	445	530	480
Activation volume for dislocation creep, V_{Disloc} (cm^{-3}/mol)	0	0	13	10
Pre-exponential constant for Peierls creep , log($B_{Peierls}$) (Pa^{-n} s^{-1})	-	-	11.76	-
Activation energy for Peierls creep, $E_{Peierls}$ (kJ / mol)	-	-	540	-
Peierls stress, $\tau_{Peierls}$ (GPa)	-	-	8.5	-

Table 1: Model parameters. *Dislocation creep parameters for upper crust: wet quartzite (Gleason & Tullis 1995), lower crust: Pikwitonian granulite (Wilks & Carter 1990), lithospheric mantle: dry olivine (Hirth & Kohlstedt 2003), asthenospheric mantle: wet olivine, i.e. 500 ppm H/Si (Hirth & Kohlstedt 2003). Peierls creep parameters for mantle: (Kameyama et al. 1999). *the friction coefficient decreases linearly by 90 % of the initial value when plastic strain reaches 1, and remains constant for larger strains.*

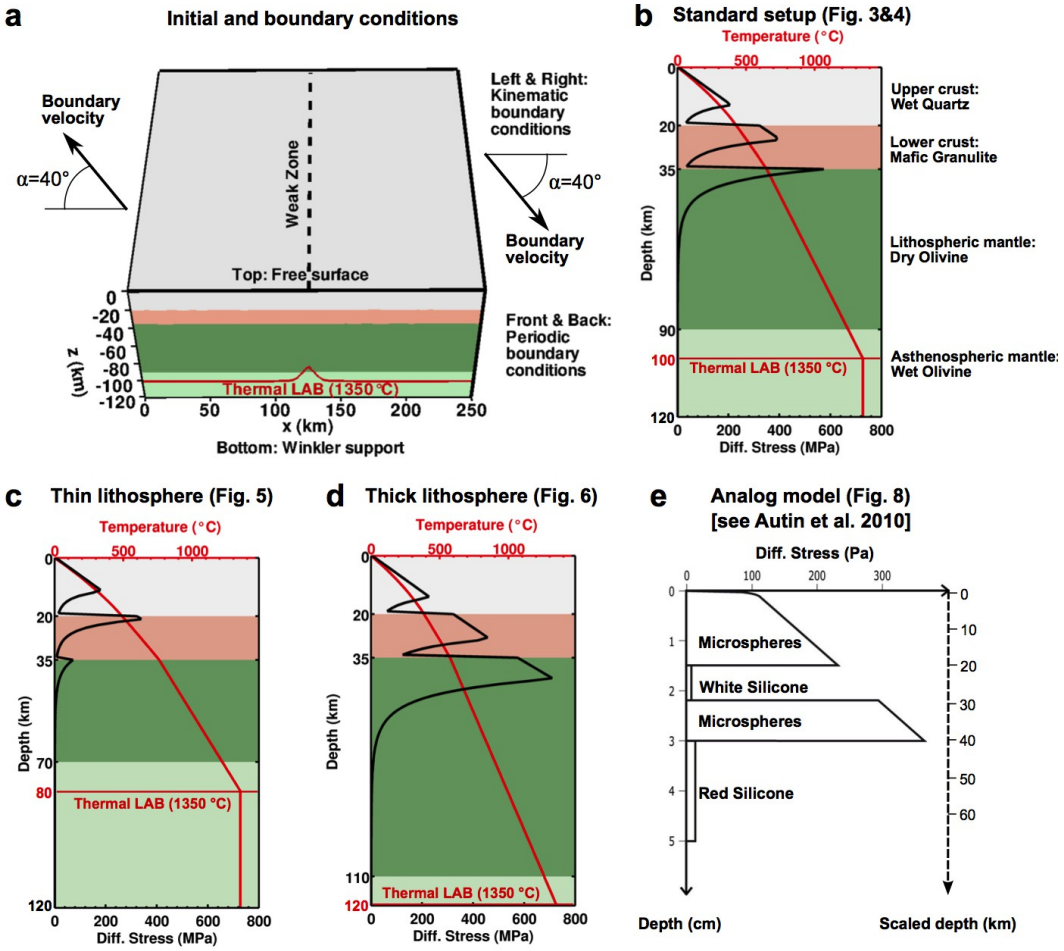

Figure 2: Model setup. ***(a)*** *Boundary conditions: Extensional velocities are prescribed at the boundaries in x-direction. The angle of obliquity α is defined as the angular difference between extension velocity and rift normal. Periodic boundary conditions in y-direction realize an in principle infinitely long rift zone. Starting conditions: Initially, the system is in thermal equilibrium defined by thermal material parameters as well as surface and asthenosphere temperature (0 °C and 1350 °C respectively). The thermal lithosphere-asthenosphere boundary (LAB) is situated at 100 km depth and is modified by a linear seed in the model centre.* ***(b-c)*** *The thickness of the material layers and the LAB depth define both the temperature and stress distribution at model start.* ***(e)*** *Initial yield strength profile of the analogue model (Autin et al. 2010).*

We define the angle of obliquity α as the angle between boundary velocity direction and the rift normal. In this study, we use α=40° which is representative for the obliquity encountered in the Gulf of Aden where extension direction and rift normal are oriented N025°E and N015°W, respectively. Extensional rates of the Miocene Gulf of Aden rift system are poorly constrained. Here we assume a full extension velocity of 10 mm/yr that is incorporated in our simulations through velocity boundary conditions at the model sides facing in *x*-direction so that they move symmetrically with 5 mm/yr. The model velocity is equivalent to 10 km/My which results in a maximum extension of 200 km after 20 My model time. The two sides of the model facing in *y*-direction are connected via periodic boundary conditions which effectively realises an infinitely long rift zone. The free surface boundary conditions at the upper model face allows self-consistent evolution of topography. At the lower model boundary, isostatic equilibrium is realized by means

of the Winkler boundary condition (e.g. Gerya 2009). During remeshing, the lower boundary surface is reset to 120 km while new numerical markers are introduced allowing for inflow of asthenospheric material through the bottom surface.

We apply the finite element code SLIM3D (Semi-Lagrangian Implicit Model for 3 Dimensions; Popov and Sobolev 2008) to solve the coupled conservation equations of momentum

$$-\frac{\partial p}{\partial x_i}+\frac{\partial \tau_{ij}}{\partial x_j}+\rho g_i=0 \tag{1}$$

energy

$$\rho C_p\frac{DT}{Dt}=\frac{\partial}{\partial x_i}\left(\lambda\frac{\partial T}{\partial x_i}\right)+\tau_{ij}\dot{\varepsilon}_{ij}+\rho A \tag{2}$$

and mass

$$\frac{1}{K}\frac{Dp}{Dt}-\alpha_T\frac{DT}{Dt}+\frac{\partial v_i}{\partial x_i}=0 \tag{3}$$

with coordinates x_i, time t, material time derivative D/Dt, velocities v_i , temperature T, pressure p, stress deviator τ_{ij}, strain rate deviator $\dot{\varepsilon}_{ij}$, density ρ, gravity vector g_i, heat capacity C_p, heat conductivity λ, thermal expansivity α_T , radioactive heat production A, and bulk modulus K. The Einstein summation rule applies for repeated indices.

Mechanical material properties are introduced by decomposing the deviatoric strain rate tensor into an elastic, viscous, and plastic component (Simo and Hughes, 2000)

$$\dot{\varepsilon}_{ij}=\dot{\varepsilon}_{ij}^{elastic}+\dot{\varepsilon}_{ij}^{viscous}+\dot{\varepsilon}_{ij}^{plastic}=\frac{1}{2G}\hat{\tau}_{ij}+\frac{1}{2\eta_{eff}}\tau_{ij}+\dot{\gamma}\frac{\partial Q}{\partial \tau_{ij}} \tag{4}$$

with the elastic shear modulus G, the objective stress rate τ_{ij} , the effective creep viscosity η_{eff}, the plastic multiplier $\dot{\gamma}$, and the plastic potential function Q.

The effective creep viscosity is computed using the flow laws for diffusion, dislocation, and Peierls creep (Kameyama et al. 1999):

$$\eta_{eff}=\frac{1}{2}\tau_{II}\left(\dot{\varepsilon}_{Diff}+\dot{\varepsilon}_{Disloc}+\dot{\varepsilon}_{Peierls}\right)^{-1} \tag{5}$$

where τ_{II} denotes the second invariant of deviatoric stress. Individual flow law formulations are:

Diffusion creep

$$\dot{\varepsilon}_{Diff}=B_{Diff}\tau_{II}\ \exp\left(-\frac{E_{Diff}+pV_{Diff}}{RT}\right) \tag{6}$$

Dislocation creep

$$\dot{\varepsilon}_{Disloc} = B_{Disloc} (\tau_{II})^n \exp\left(-\frac{E_{Disloc} + pV_{Disloc}}{RT}\right) \quad (7)$$

Peierls creep

$$\dot{\varepsilon}_{Peierls} = B_{Peierls} \exp\left[\frac{-E_{Peierls}}{RT}(1-\beta)^2\right]\left[\frac{\tau_{II}}{\beta \tau_{Peierls}}\right]^{(2\beta(1-\beta)\frac{E_{Peierls}}{RT})} \quad (8)$$

The Mohr-Coulomb model is used for implementation of plastic failure:

$$F = \frac{1}{2}(\sigma_{max} - \sigma_{min}) + \frac{1}{2}(\sigma_{max} + \sigma_{min})\sin\phi - c\cos\phi \leqslant 0 \quad (9)$$

with the yield surface F, maximum and minimum principal stresses σ_{max} and σ_{min}, friction angle φ, and cohesion c. All parameter values are explicitly listed in Table 1. Additional information on SLIM3D and its applications can be found in Popov and Sobolev (2008), Brune et al. (2012), Brune et al (2013), Quinteros et al. (2010), Quinteros and Sobolev (2012), Melnick et al. (2012), Popov et al. 2012, as well as Quinteros and Sobolev (2013).

In many cases oblique rifting arises because inherited lithospheric weak zones like sutures are reactivated with an oblique extensional component (Ziegler and Cloetingh, 2004). We introduce a weak zone by implementing a small linear temperature heterogeneity in the centre of the prospective rift (Fig. 2a). In doing so we anticipate a small amount of lithospheric necking that focuses the extensional deformation into the desired rift axis. This is one possible way of rift initialization. Alternative means are mechanical anisotropy (Tommasi and Vauchez, 2001), implementation of a weak plastic seed (Huismans and Beaumont, 2003), or crustal thickening (van Wijk, 2005). Note that after a small amount of extension, all of these techniques will result in lithospheric necking comparable to our initial condition.

Three weakening mechanisms are reproduced in the model. (i) Friction softening is introduced using a strain-dependent effective friction coefficient that decreases linearly from 0.6 to 0.06 for plastic strains between 0 and 1 while it remains constant at 0.06 for plastic strains larger than 1. (ii) Shear heating results in increased temperature that is proportional to stress multiplied by strain rate. (iii) Dislocation creep intrinsically results in strain rate softening due to the stress exponent n>1 which leads to localizes viscosity reduction.

2.2. Stress interpretation method

In most geodynamic codes (including SLIM3D), fault structures are represented by finite width shear bands that localize with a width of several elements. Hence, fine-scale fault patterns that are visible both in nature and in analogue models are difficult to reproduce in relatively coarse 3D models. We address this problem by using a simple post-processing technique that uses the stress tensor at the model surface in order to infer stress regime and fine-scale fault azimuths. This technique extracts additional information from the model which widens the interpretation scope of the numerical experiments.

The stress interpretation method is based on the classic knowledge that all shear stress components are zero at the surface of the Earth, so that one principal stress component has to be

oriented vertically which allows to classify the stress regime either as extensional, strike-slip, or compressional (Anderson 1948). In locally isotropic and homogeneous media, the fault azimuth and fault type (normal, strike-slip, thrust) directly reflect the local stress field. The stress interpretation method operates in two distinct steps: (i) Representing the stress regime at each surface element (ii) Evaluating the optimally oriented fault direction. Both steps are described in detail in the next paragraphs.

2.2.1 Representing the stress regime at each surface element

We visualize the stress regime using the scalar Regime Stress Ratio (RSR) that indicates extension, strike-slip motion and compression on a continuous scale (Simpson 1997). A similar technique involving the non-dimensional Argand Ratio has been successfully applied to interpret stress states in thin sheet models (England and McKenzie, 1982; Houseman and England, 1986; Rey and Houseman, 2006). The difference between Argand Ratio and RSR and is that the latter is confined to the interval between 0 and 3 which allows direct association of all possible stress regimes as shown in Table 2.

In order to evaluate the RSR value at each surface element, we first compute the principal stress components, i.e. the eigenvalues σ_1, σ_2, σ_3 of the stress tensor. Together with the corresponding eigenvectors we identify σ_v, σ_h, σ_H, the vertical, smallest horizontal, and largest horizontal stress component, respectively. Further, we define the index n

$$n=\begin{cases} 0 & if \quad \sigma_h<\sigma_H<\sigma_v \quad (normal\ faulting) \\ 1 & if \quad \sigma_h<\sigma_v<\sigma_H \quad (strike-slip\ faulting) \\ 2 & if \quad \sigma_v<\sigma_h<\sigma_H \quad (thrust\ faulting) \end{cases}$$

and the ratio R between smallest and largest differential stress (Bott 1959).

$$R=\left(\frac{\sigma_2-\sigma_3}{\sigma_1-\sigma_3}\right)$$

The RSR value itself is defined as

$$RSR=(n+0.5)+(-1)^n(R-0.5)$$

and the physical meaning of this value is listed in Table 2.

RSR-value	0.5	1	1.5	2	2.5
Meaning	Extension	Transtension	Strike-slip	Transpression	Compression

Table 2: Meaning of the Regime Stress Ratio (RSR). *The RSR value is a scalar value that is continuous between 0 and 3. It is used to infer stress regimes and their associated fault types from stress tensors.*

2.2.2 Optimal fault orientation

Based on the local stress field, we infer an optimally oriented fault direction at each surface element. Assuming isotropic and homogeneous materials, we follow the standard procedure of Andersonian faulting where both extensional and compressive stress regimes result in σ_3-orthogonal fault azimuths while strike-slip faults occur at $\pm\varphi_{eff}$ from σ_1 (with the effective friction angle φ_{eff}=31°). Azimuth is measured as the clockwise angle from northward direction.

In analogue experiments and field surveys, the relative importance of individual fault families can be expressed in terms of cumulated fault length, whereas in our numerical model, we simply count the number of elements that belong to a specific azimuth range. In contrast to analogue models, our method allows to directly discriminate between strike-slip, normal, and thrust faults. For strike-slip faults, however, stress tensor information alone does not suffice to differentiate between dextral and sinistral conjugates. Hence, we depict the conjugate fault families in two different clusters that are scaled by a factor of 0.5 so that the overall number of evaluated elements is not affected.

The stress interpretation method allows to compute stress regime and fault azimuth for any stress tensor at the model surface, even though the considered element experiences no strain at all. Hence, it is necessary to exclude the quasi non-deforming elements outside the rift zone from the analysis. We therefore restrict our analysis to the zone of tectonic activity, where the strain rate exceeds 10^{-15} s^{-1}. This number is somewhat arbitrary, but the overall results are not affected if the threshold value is changed within reasonable range. This is due to the fact the area of high tectonic surface activity becomes very well constrained shortly after model start (Fig. 3a). Note that the extent of the active region successively localises towards the rift centre. Therefore, the overall number of elements that experience high strain rate and that contribute to the analysis decreases with time. This number is indicated for each time step in the upper left corner of the azimuth diagram.

The fundamental assumption of this method is that the stress state dictates fault geometry. However, this is only true for homogeneous, isotropic media. In natural settings, inherited faults are common and reactivation may occur which may lead to non-Andersonian fault geometries. Moreover, the method accounts only for incremental faulting as no information on previous small-scale fault geometry is inherited to the next time step. In the strict sense, the assumption that one principal stress is oriented perpendicular to Earth's surface does not hold true if strong topographic gradients exists. This limitation should be remembered during stress interpretation at rift shoulders, although due to smooth topography variation in our model, local gradients are relatively small. Keeping these drawbacks in mind, it is one aim of this article to investigate the scope of this method by comparing its results to analogue experiments and the Gulf of Aden rift system.

3. Numerical model results

3.1. General deformation pattern

The strain rate plots of Fig. 3a depict finite-width shear zones with a typical width of few elements. The spontaneous formation of shear zones takes place within the first computational time steps. Due to strain softening, shear zones become weaker with accumulated deformation so that individual small-scale shear zones compete and their number reduces with time.

The largest amount of deformation is taken up by shear zone parts atop the lithospheric necking domain. During the first 6 My large conjugate normal faults develop within the shear zones that cut through the whole crust (Fig. 3b). During continued rifting, the distance of the conjugate faults at the surface is reduced with time until it vanishes and break-up takes place at 14 My. This model does not account for petrophysical formation of oceanic crust so that continental break-up is assumed to occur when the lithosphere is broken and asthenospheric material reaches the surface.

Three fault azimuths play a fundamental role during the discussion of the model, i.e. rift-parallel (N075°E), displacement-orthogonal (N115°E), and intermediate (N095°E). We discuss the processes that underlie each direction in Section 5.3.

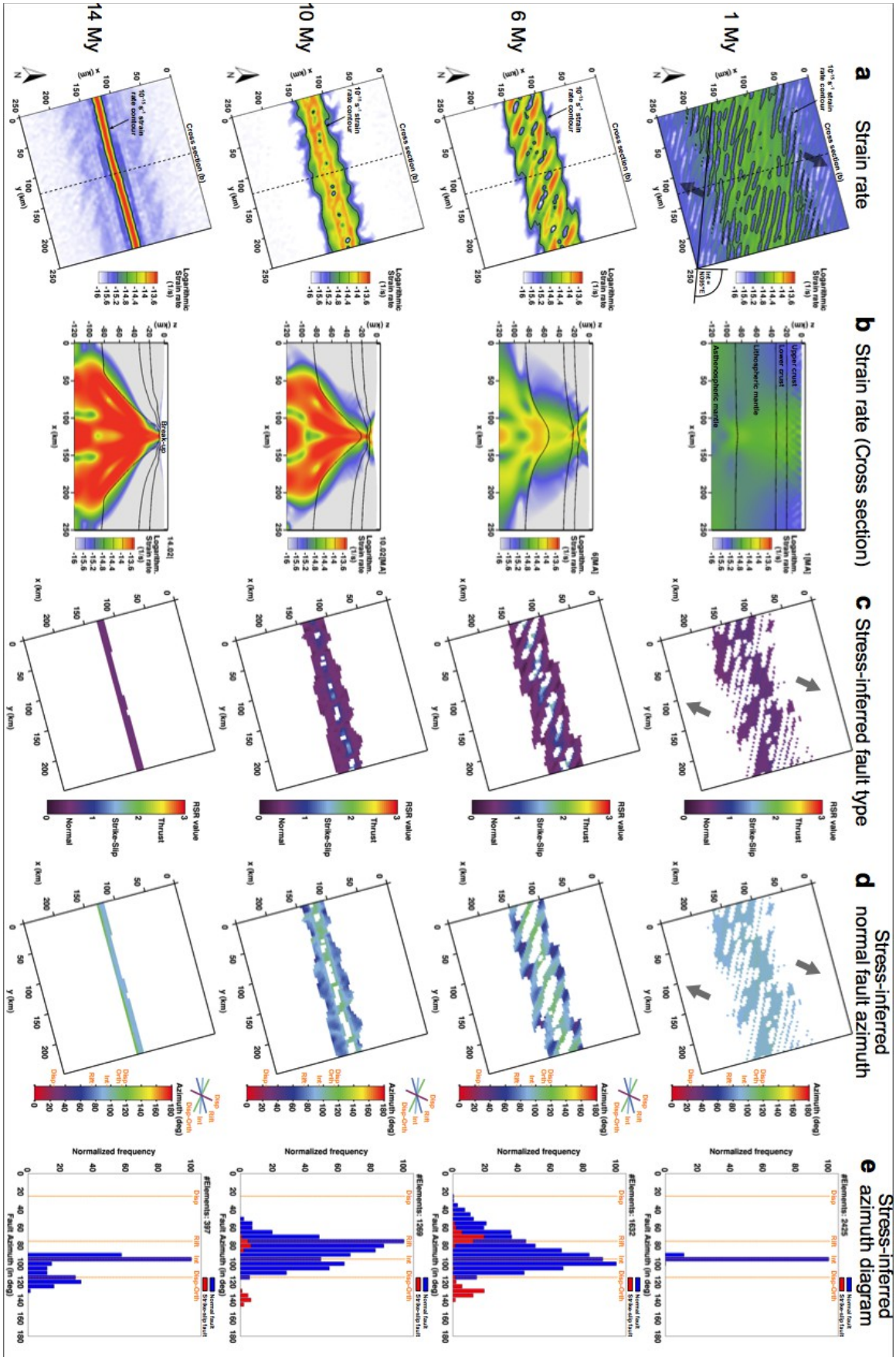
a Strain rate
b Strain rate (Cross section)
c Stress-inferred fault type
d Stress-inferred normal fault azimuth
e Stress-inferred azimuth diagram
1 My
6 My
10 My
14 My
Cross section (b)
Upper crust
Lower crust
Lithospheric mantle
Asthenospheric mantle
Break-up
Normal
Strike-Slip
Thrust
Normalized frequency
Fault Azimuth (in deg)

Figure 3: Standard scenario evolution. *Model evolution at 1 My, 6 My, 10 My, and 14 My (i.e. 10 km, 60 km, 100 km, and 140 km extension, respectively).* ***(a)*** *Surface strain rate pattern. Initially, shear zones are parallel to the expected intermediate azimuth of N095°E. At 6 My a complex en-echelon pattern occurs.* ***(b)*** *Mid-model cross section strain rate cross section as shown in (a). Black lines indicate boundaries between material layers. Lithospheric necking and crustal faults localize toward the rift centre until break-up occurs at 14 My.* ***(c)*** *The stress tensor of each surface element is visualized in terms of stress regime. White areas experience negligible tectonic deformation (strain rate < 10^{-15} s^{-1}, see contour in (a)) and are excluded from the stress analysis. Normal faulting is the dominant mechanism except for a temporary strike-slip region in the rift centre.* ***(d)*** *In places where the stress regime indicates normal faulting, we plot the normal fault azimuth. The en-echelon pattern at 6 My strongly effects local stress orientations.* ***(e)*** *Frequency diagram of stress-inferred normal and strike-slip fault azimuths. The amplitude is normalized by the number of elements inside the tectonically active region (see contour in (a)). Note that figures showing the whole evolution in steps of 1 My can be found in the supplementary material.*

3.2. Three-phase evolution

The evolution of the numerical model can be divided in three main phases. Note, however, that the transitions between phases are not abrupt but take place over one or two My. Figures showing the evolution in steps of 1 My can be found in the supplementary materials.

Phase 1. (1-5 My): At 1 My, the strain rate pattern of Fig. 3a shows small-scale shear zones that strike at an angle of N095°E azimuth that is intermediate between the displacement-orthogonal direction and the rift orientation. Within few million years, they develop into an en-echelon system with a wavelength of several tens of kilometres. The stress regime (Fig. 3c), is of extensional type everywhere and shows optimal fault orientation with intermediate directions (Fig. 3d,e).

Phase 2. (6-13 My): Deformation of the en-echelon shear zones strongly localises towards the lithospheric necking region (Fig. 3a). The normal fault azimuth map (Fig. 3d) shows that the en-echelon structure features a complex stress pattern: At the rift border, rift-parallel and intermediate normal faulting takes place. Simultaneously, strike-slip faults and displacement-orthogonal normal faults occur in the rift centre that delimit individual shear zones (Fig. 3c,d). The azimuth diagram shows a shift from intermediate to rift-parallel directions and even involves fault azimuths that are smaller than N075°E. At 10 My, rift-parallel faults are dominant at the rift borders and a strong localization of the deformation towards the rift centre reoccurs while the en-echelon pattern vanishes.

Phase 3. (14 My and after): Incipient break-up links the individual shear zones. Instead of multiple ridge segments that are offset by ridge-orthogonal fracture zones, our model produces a single straight ridge oblique to extensional direction. This mode of oblique sea-floor spreading is known from slow and ultra-slow mid-oceanic ridges (Montési and Behn, 2007) whereby our extension rate of 10 mm/yr satisfies the condition for ultra-slow spreading (< 12 mm/yr, Dick et al. 2003). However, the tendency of the system to produce the rectangular ridge-transform spreading pattern can be seen in the stress-inferred azimuth diagram (Fig. 3e at 14 My), where displacement-orthogonal faults are visible together with intermediate fault directions during break-up of the lithosphere.

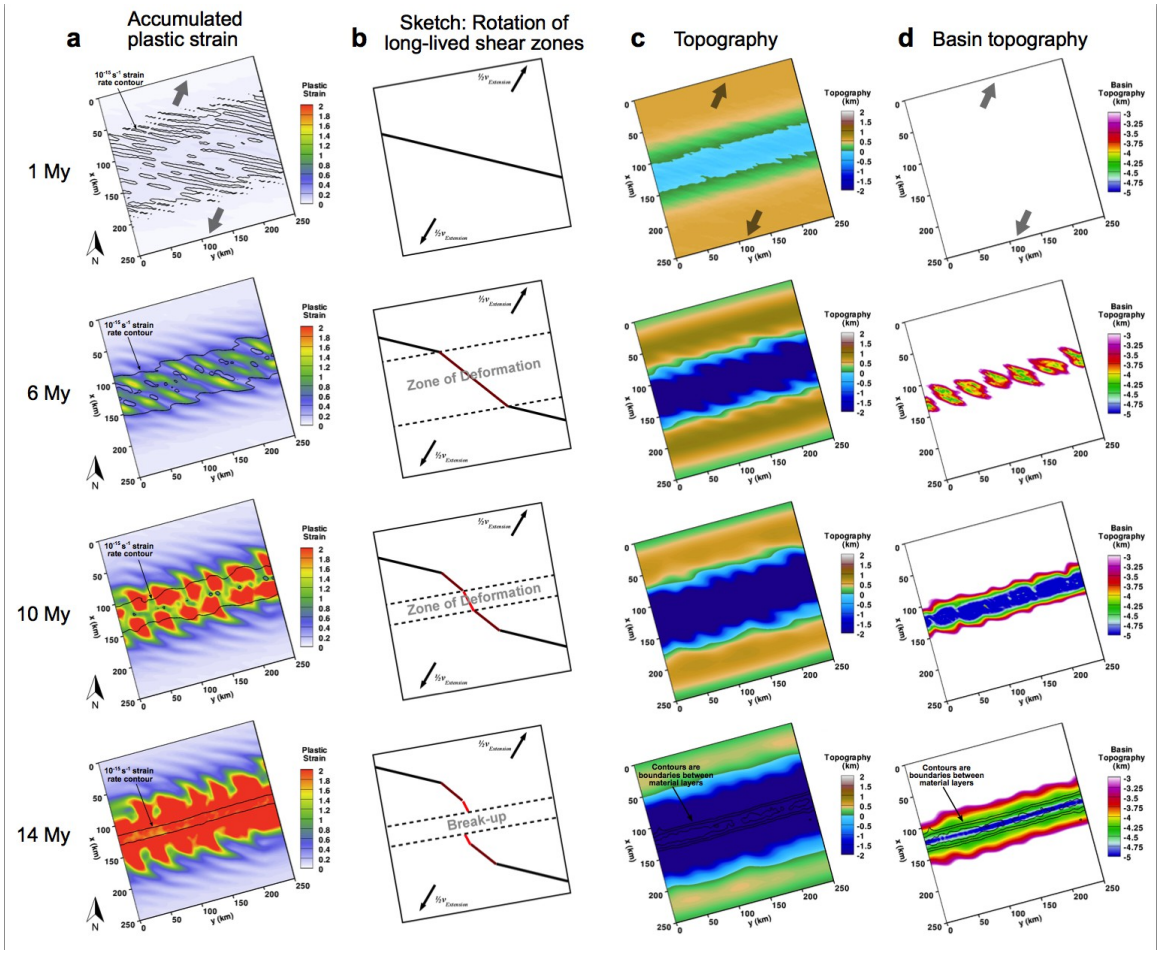

***Figure 4**: **Strain and topography patterns of the standard scenario.** **(a)** The accumulated plastic strain shows formation of sigmoidal deformation patterns. The active region is outlined by the strain rate contour. **(b)** Illustration of how long-lived shear zones generate sigmoidal strain patterns. **(c)** Topography shows rift shoulder uplift due to hot asthenospheric upwelling at 6 My followed by subsidence due to lithospheric cooling. **(d)** The geometry of the basins is controlled by shear zone location and wavelength. Note that figures showing the whole evolution in steps of 1 My can be found in the supplementary material.*

The final strain distribution (Fig 4a at 14 My) shows sigmoid deformation patterns. The sigmoidal shape can be explained by successive rift localisation and the longevity of individual shear zones: After formation of the initial en-echelon pattern, the central portion of each shear zone gets stretched parallel in direction of extension which appears as a clockwise rotation (Fig. 4b). Since deformation localizes towards the rift centre, the area where rotation occurs narrows with time. Thus, shear zones of the proximal margin experience less rotation while distal margin shear zones are deformed until they are nearly parallel to the direction of extension.

3.3. Alternative model setups and robustness of results

In this section we study the robustness of our results. We therefore change the initial configuration of the model by (i) decreasing and (ii) increasing the lithosphere-asthenosphere boundary depth followed by (iii) a model run with two times coarser numerical resolution.

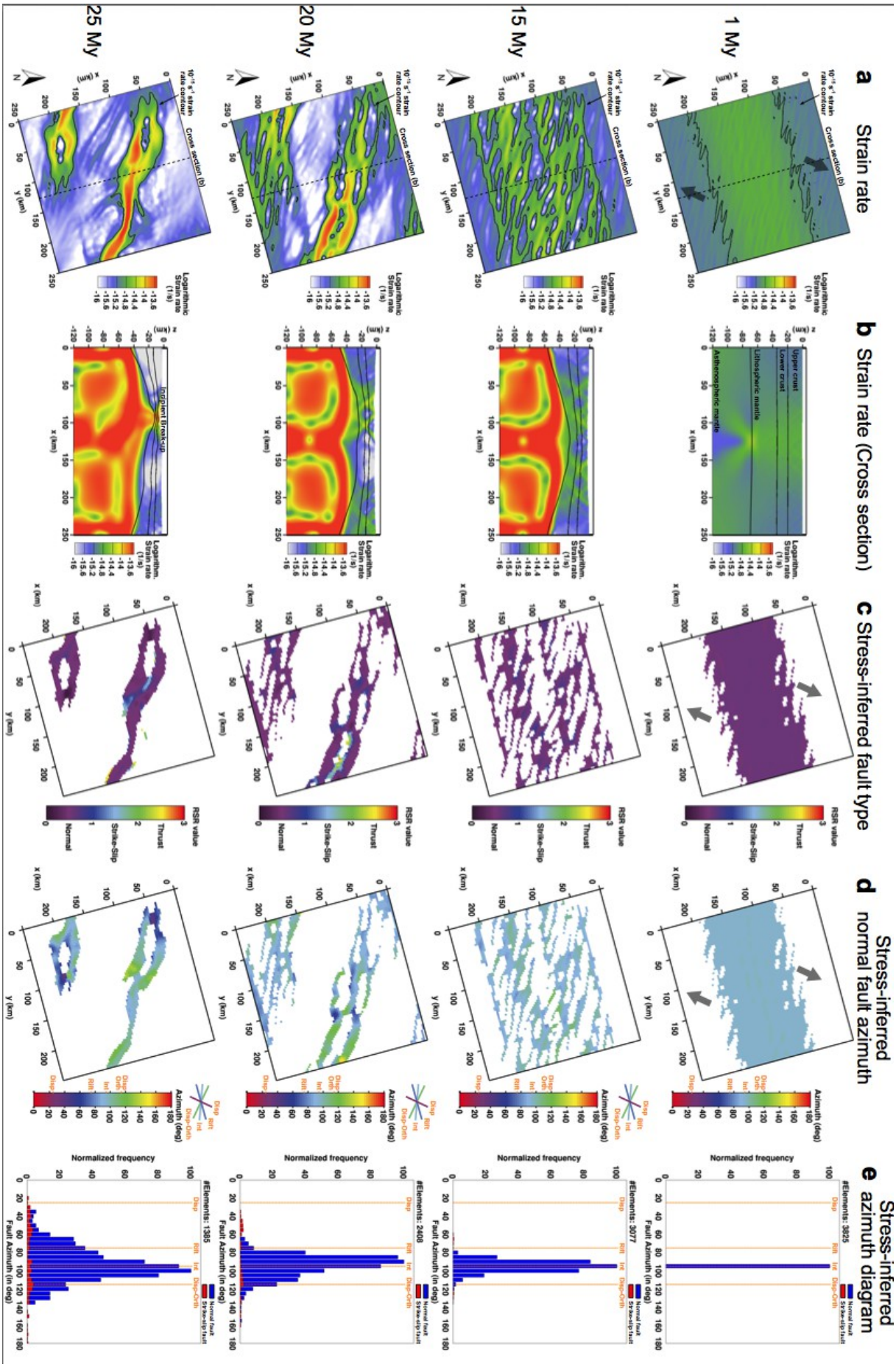
a Strain rate
b Strain rate (Cross section)
c Stress-inferred fault type
d Stress-inferred normal fault azimuth
e Stress-inferred azimuth diagram
1 My
15 My
20 My
25 My
Upper crust
Lower crust
Lithospheric mantle
Asthenospheric mantle
Incipient Break-up
Normal
Strike-Slip
Thrust
Azimuth (deg)
Normalized frequency
Fault Azimuth (in deg)

Figure 5: Alternative setup with thin lithosphere (80 km). *The initial strength distribution of this scenario is shown in Fig. 2c. Viscous rheology dominates the rift system and significantly prolongs the rift process, so that break-up takes place 10 My later than in the standard scenario. Described phases of the standard scenario are not applicable to this model. Localisation proceeds without en-echelon pattern towards large displacement-orthogonal structures (20 and 25 My). Normal fault azimuths involve rift-parallel, intermediate and displacement-orthogonal directions.*

Changing the LAB depth severely affects the initial strength distribution through the vertical temperature profile at model start: A shallow thermal LAB of 80 km (instead of the previously used 100 km) results in a weak mantle lithosphere and involves less brittle deformation within the crust (Fig. 2c). On the contrary, a thick lithosphere of 120 km produces both strong crust and mantle (Fig. 2d). In that case, crustal deformation is dominated by brittle failure. In both scenarios, we initiate the chemical LAB (i.e. the boundary between dry and wet olivine rheology) 10 km above the thermal LAB.

Initially, the model with 80 km deep thermal LAB does not involve localised shear zones as in the previous simulation: At 1 My, the strain rate is much more distributed both at the surface (Fig. 5a) and in depth (Fig. 5b). This is due to the fact that the viscously deforming crustal domain is much thicker than the brittle portions of the crust. Consequently, brittle strain softening is less efficient in focussing deformation into discrete shear zones. After 15 My, a wide necking zone evolves and individual shear zones emerge with intermediate (N095°) orientations that are visible both in surface strain rate (Fig. 5a) and stress-inferred fault azimuth (Fig. 5d). These shear zones successively merge into two large zones of deformation that are oriented in displacement-orthogonal direction. Individual segments of the shear zones with a specific orientation display the respective normal fault azimuth (Fig 5d at 25 My): Displacement-orthogonal parts, for example show displacement-orthogonal fault orientations. During break-up at 25 My, the surface shear zones strongly resembles offset mid-ocean ridge segments. Note that these displacement-orthogonal ridges occur in the thin-lithosphere model but not in the standard scenario. The reason probably lies in the relationship of plate strength and the length of ridge segments. If plates are strong, mid-oceanic ridge segments are long, whereas weak plates with low effective viscosity generate short segments (Gerya, 2010 and references therein). Thus, the setup with hotter and hence weaker lithosphere can produce smaller ridge segments that fit into the modelling domain, while a larger model size would be needed to observe segmentation in the standard scenario.

The model with 120 km thick lithosphere is strongly controlled by brittle localisation (Fig. 6). The overall evolution is very similar to the standard scenario with 100 km deep thermal LAB. Distinct parallel shear zones are present at 1 My with intermediate orientation that interconnect in depth to a highly symmetric fault network (Fig. 6a,b). Deformation localises into the rift centre and forms several large shear zones that interconnect via en-echelon pattern. Simultaneously, the stress-inferred fault azimuth shifts towards rift-parallel orientation while strike-slip domains emerge between the shear zones. The overall azimuth pattern shows a higher complexity than the standard scenario incorporating all possible fault orientations. During break-up all strain is taken up by a single straight shear zone in the model centre and the stress-inferred fault diagram indicates intermediate and displacement-orthogonal fault azimuths. The spacing between individual shear zones and the width of associated basins results from a dynamic interplay involving the brittle-ductile transition depth in the upper crust (e.g. Vendeville et al. 1987), the strength contrast between upper and lower crust (Wijns et al. 2005) and the lithospheric necking width. For example, the deeper brittle-ductile transition depth in the thick-lithosphere model at 1 My and 8 My (Fig. 6) allows to accommodate less shear zones than the standard scenario (Fig. 3) so that specific basins must have a larger wavelength.

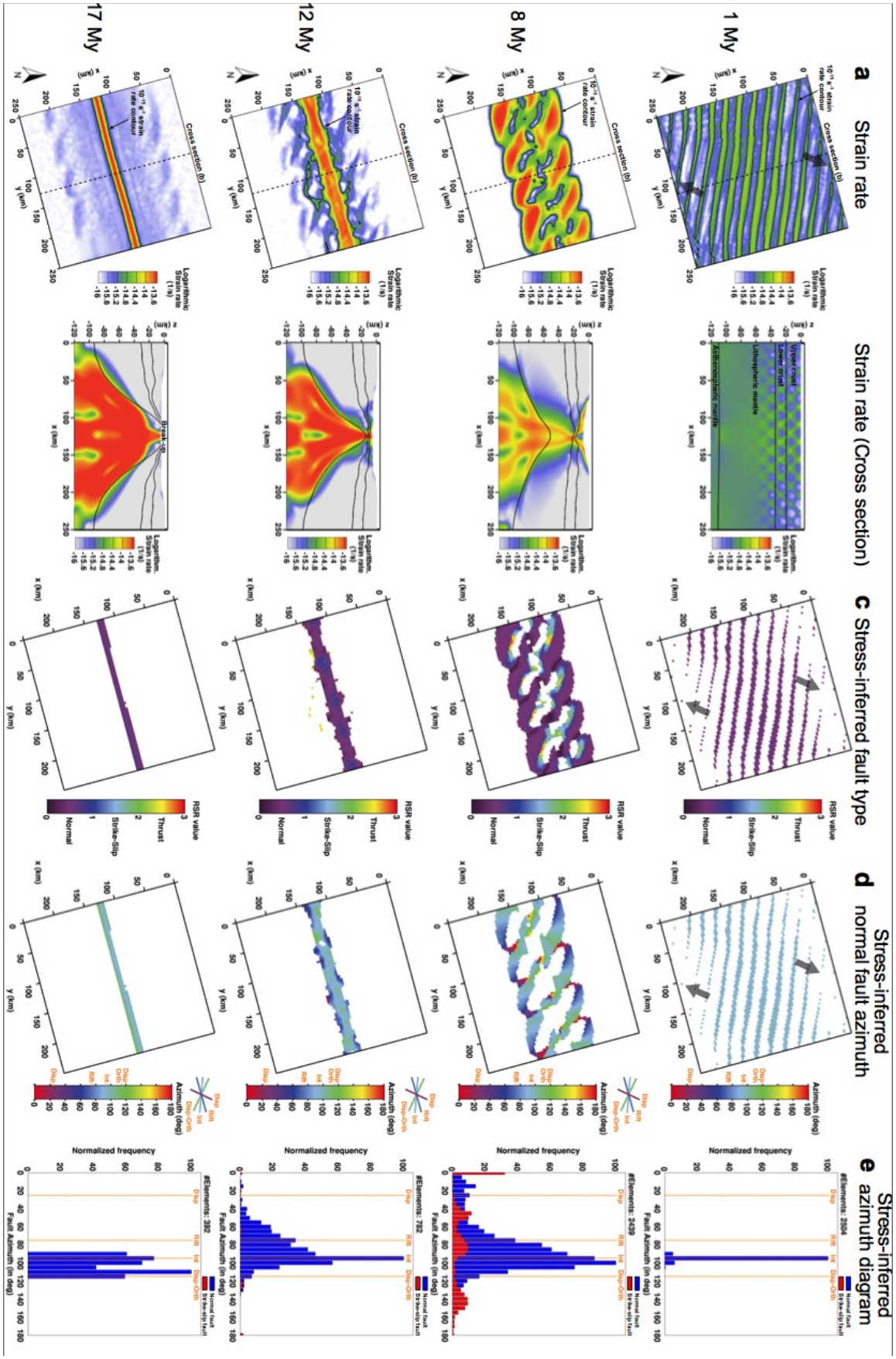
a Strain rate
Strain rate (Cross section)
c Stress-inferred fault type
d Stress-inferred normal fault azimuth
e Stress-inferred azimuth diagram
1 My
8 My
12 My
17 My
Cross section (b)
Upper crust
Lower crust
Lithospheric mantle
Asthenospheric mantle
Break-up
Logarithmic Strain rate (1/s)
RSR value
Normal
Strike-Slip
Thrust
Azimuth (deg)
Normalized frequency
Fault Azimuth (in deg)
Disp
Rift
Int
Disp-Orth
Normal fault
Strike-slip fault

Figure 6: Alternative setup with thick lithosphere (120 km).
The initial strength distribution of this scenario is shown in Fig. 2d. Although crustal faulting is much more pronounced than in the standard scenario, overall rift evolution involves the described three phases. Stress rotations in the en-echelon zone at 8 My are more complex than in the standard model systematically involving all possible fault directions.

In order to evaluate the influence of model resolution on our results, we modify the standard scenario by two times coarser resolution (i.e. 6 km element length instead of 3 km, Fig. 7). The overall rift evolution is similar to the original model. Although the shear zones are more diffuse both in the map view and the cross section, both the necking width and general timing correspond very well. Strong similarity exists in variables that have been inferred through the stress-interpretation technique: We find predominantly normal faulting with intermediate orientation in Phase 1, a strong tendency towards rift-parallel faulting during Phase 2 and intermediate to displacement-orthogonal azimuths upon break-up. Differences to the standard model involve the less well expressed strike-slip populations during phase 2 and that displacement-orthogonal azimuths are less expressed during break-up. In quintessence, this experiment shows that the overall model evolution is relatively independent of model resolution. Moreover, we argue that stress-inferred variables allow resolution-independent conclusions.

3.4. Model limitations

Note that the model capabilities are limited in several aspects. Most importantly, magma migration and dike formation that tend to decrease lithospheric strength perpendicular to the direction of extension are not accounted for. Surface processes like erosion and sedimentation are not included. Besides, the limits of computational power restrict our model resolution to 3 km which is still far from resolving individual faults. Nevertheless, the presented model is one of the first that reproduces lithospheric-scale rift evolution from initial deformation until break-up.

4 Numerical model vs. Gulf of Aden analogue model

Before we compare the numerical model to the Gulf of Aden, we will explore differences and similarities to the previously conducted lithospheric-scale analogue model of Autin et al. (2010) that also featured an obliquity of 40°. As the numerical model uses a prescribed weakness in the lithosphere, we compare it to an analogue experiment which also contains a pre-existing lithospheric weakness (Fig. 8).

The analogue model is constructed in order to reproduce oblique rifting by way of shifted lateral velocity discontinuities (see Autin et al., 2010 for details). Moreover, an oblique weakness trends parallel to the direction of obliquity imposed by the lateral velocity discontinuities, and joins them. The model involves a four-layer type lithosphere strength profile (shown in Fig. 2e) modelled using granular materials and silicone. This modelled lithosphere overlies a low viscosity, higher density glucose syrup that mimics the asthenosphere. Lateral dimensions of the setup (56 cm times 30 cm in the laboratory) scale to 750 km times 400 km in reality. The maximum extension of the model is 20 % which corresponds to 80 km if scaled to natural dimensions or to 8 My of our numerical model evolution.

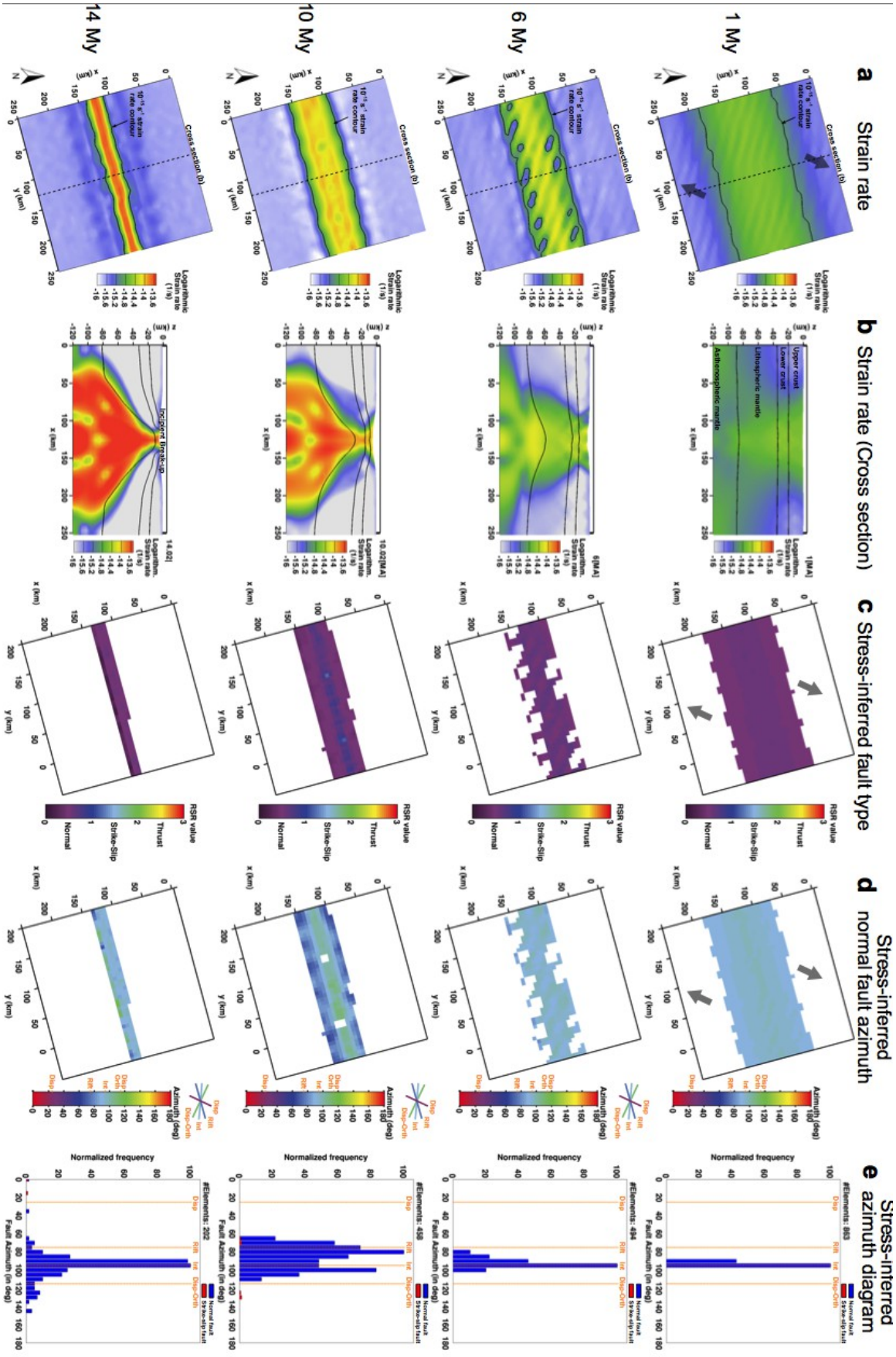
a Strain rate
b Strain rate (Cross section)
c Stress-inferred fault type
d Stress-inferred normal fault azimuth
e Stress-inferred azimuth diagram
1 My
6 My
10 My
14 My
Cross section (b)
Upper crust
Lower crust
Lithospheric mantle
Asthenospheric mantle
Incipient Break-up
Normal
Strike-Slip
Thrust
RSR value
Disp
Rift
Int
Disp-Orth
Azimuth (deg)
Normalized frequency
Fault Azimuth (in deg)
Normal fault
Strike-slip fault

Figure 7: Low-resolution model (6 km element size).
Although distinct shear zones are more diffuse than in the standard scenario, the overall model evolution is very similar in terms of timing, deformational structures and normal fault orientations.

Autin et al. (2010), as well, observe the three main fault populations: rift-parallel, intermediate, and displacement-orthogonal. Moreover, the proposed three steps of development are very similar to the ones observed in the numerical models (Fig. 8): (i) The fault populations, especially during the early stages of deformation, are composed of intermediate faults. This fault population is characteristic for oblique rifts as observed in previous studies. (ii) In later stages, faults parallel to the rift become numerous and are located in the rift borders where thinning is most important. (iii) During the final stages of extension, the small-scale deformation pattern is composed of displacement-orthogonal faults in the deepest parts, i.e. in the rift centre.

Although the three stages are similar to the ones observed in the numerical models, several differences exist: The numerical model indicates that during the Phase 1, only intermediate faults develop, whereas displacement-orthogonal faults develop also in the analogue model. However, these orientations occur near the model boundary and might hence be related to boundary effects. Phase 3 of the numerical model displays displacement-orthogonal as well as intermediate faults (Fig. 3d), whereas Autin et al. 2010 infer that only displacement-orthogonal faults form in the analogue models at this stage. Unfortunately, the advanced deformation inhibited precise measurements of the fault lineaments and no statistic plot is available for this stage. In the numerical model, this stage is controlled by the ascent of the hot asthenosphere and subsequent plate cooling, which cannot be reproduced in analogue models. These processes induce a strong localization of the deformation, where oblique weakening combined with the far-field stress could lead to intermediate fault development. The azimuth diagram (Fig. 3e) shows clearly displacement-orthogonal faults at 14 My, when the break-up occurs. This is different from the analogue model, which suggests that they appear at earlier stages. It is noteworthy that clockwise rotations of the structural pattern start at 7 My in the numerical model. Rotations are observed in the analogue models and result in the same general sigmoid pattern.

Another fundamental similarity between both models is the location of those faults with similar azimuth. In the numerical and the analogue models, rift-parallel faults are always located along the rift flanks. This is where the overall oblique thinning of the lithosphere creates a strong lateral density contrast between the dense lithosphere and the hot ascendant asthenosphere. These variations are thought to induce an extensional force component perpendicular to the rift flanks (Bellahsen et al., this volume). On the contrary, displacement-orthogonal faults are always created in the rift centre where the lateral density contrast is much smaller.

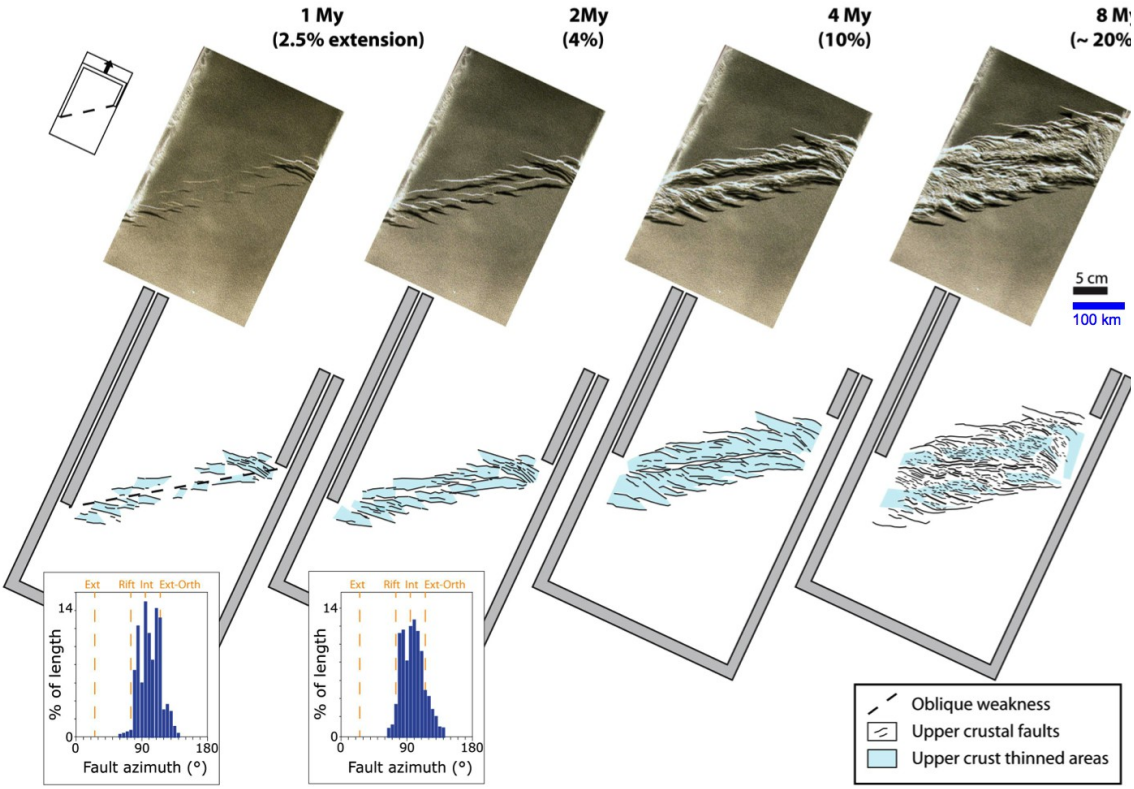

Figure 8: Analog model evolution. *Top view photographs and interpretations of the lithosphere-scale analogue model with four brittle and ductile layers. In agreement with the numerical model, the analog model evolves in distinct phases whereby rift-parallel orientations occur at the rift flanks while intermediate and displacement-orthogonal fault directions dominate the rift centre.*

5 Numerical model vs. Gulf of Aden natural rift

5.1 Chronology and localisation of the fault populations

First we compare the distribution of the fault populations in the rift and their chronology. As described in Bellahsen et al. (this volume), the Gulf of Aden displays a general fault organisation (Fig. 1): (i) the external parts of the rift show intermediate and displacement-orthogonal faults; (ii) the rift borders focus rift-parallel faults and; (iii) the internal parts are mainly composed of intermediate fault in the OCT and displacement-orthogonal faults close to the mid-oceanic ridge. If we consider that the deformation localizes progressively towards the rift centre (e.g. Corti et al., 2003; Ring et al., 1992), then the structures of the proximal margin should be older than those of the distal one. This evolution is in accordance with the 3 step evolution of the numerical model. Indeed, Fig. 3d,e shows that (i) the intermediate faults are created first and will then be located in the external parts of the rifts; (ii) rift-parallel faults form later and are localised at the rift borders where lithospheric thinning is strongest, i.e. at 100 km and 150 km along the *x*-axis at 6 My or 110 km and 140 km at 10 My; (iii) intermediate and displacement-orthogonal faults appear in the rift centre during the final evolution of the model.

The numerical model reproduces the actual Gulf of Aden rift duration of 14 My from initial localisation to final break-up (Leroy et al. 2012). The temporal fault kinematic history of the Gulf of Aden rift system is presently still speculative. We therefore propose that the timing of our model's rift phases can be indicative for future kinematic studies of the Gulf of Aden fault evolution.

5.2 Final deformation pattern

The overall deformation pattern of the Gulf shows an en-echelon disposition of the syn-rift faults and grabens, on both side of the oblique OCT (Fig. 1a). When the Gulf is closed to the OCT (Fig 1b), the Tertiary main depocentres show en-echelon sigmoid grabens. This pattern is similar to the plastic strain pattern observed in the numerical model (Fig. 4a). The modelled basin topography is also comparable with en-echelon sigmoid basins progressively linked together and finally separated when the final localization occurs at 10-11 My (Fig 4d). Nevertheless, this en-echelon deformation occurs at larger scale (ca. 100 km) than in the numerical model (40-50 km) and is partly controlled by the Mesozoic inheritance (Ellis et al., 1996; Granath, 2001; Leroy et al., 2012; Autin et al., this volume). The wavelength difference is certainly due to the initial pattern of the inherited, widely spaced Mesozoic basins, which have focused the deformation during their reactivation, preventing the appearance of a more distributed pattern as in the numerical model. Although the main Tertiary depocentres focus in these inherited basins, deformation is also observed outside of them as for example in the Ashawq graben. Thus, it appears that the distributed deformation pattern of the model can be recognized in the Gulf of Aden but is locally controlled and enhanced by the inheritance overprinting the general pattern.

As proposed above, the sigmoid shape in the model can be due to successive rotations during ongoing extension of long-lived shear zones (Fig. 4b). In the Gulf of Aden, the inherited Mesozoic basins have a sigmoid shape and thus could have experienced such rotations. Novel analogue models that reproduce this inheritance during oblique rifting show indeed that the inherited structure ends with a sigmoid shape (Autin et al., this volume).

5.3 Processes that control major fault orientations

The intermediate fault direction (N095°E) plays a prominent role during all three phases of the model. The underlying reason for the occurrence of this orientation is the combined effect of both extensional far field stresses and its local modification by the rift zone as proposed by Withjack and Jamison (1986).

During Phase 2 (6 to 13 My), the progressive development of rift-parallel faults indicates that deformation localises along the oblique trend. The rift-parallel fault orientation can be linked to necking-related buoyancy forces that generate a rift-orthogonal stress component (Bellahsen et al., this volume): These buoyancy forces can be caused by thickness variations in the lithosphere producing lateral density variations between the dense lithosphere and the less dense, hotter ascendant asthenosphere so that the resulting force direction is perpendicular to the major lithosphere thinning (e.g. Artyushkov, 1973; Fleitout and Froidevaux, 1982). This hypothesis is supported by the localisation of rift-parallel faults in the rift borders above the maximal gradient of lithosphere thickness (Fig. 3b,d). Additionally, necking-related buoyancy has been considered an important driving force for rifting evolution even in orthogonal, 2D rift settings (Huismans et al., 2001; Davis and Kusznir, 2002; Burov, 2007). An alternative reason for rift-parallel faulting is strain partitioning between rift centre and rift flanks: Strike-slip faults emerge in the rift centre (Fig. 3c) at the same time when rift-parallel faulting occurs at the rift borders. The strike-slip zone partly accommodates the rift-parallel component of extension so that rift flanks experience only the rift-perpendicular velocity component which induces the observed rift-parallel fault direction. Strain partitioning has been observed in both natural rift systems like the Main Ethiopian Rift and corresponding analogue experiments (Agostini et al., 2011).

Deformation during the third step (from 14 My on) is localised in the rift centre. The intermediate and displacement-orthogonal faults indicate that the far-field extension dominates. The rift centre is far enough from the thinning zones (rift borders) so that the newly formed faults develop mainly in response to the far field stresses, as proposed in Autin et al. (2010). Nevertheless, the presence of intermediate faults suggests that a local stress field is still active.

The reason is probably that plate cooling takes place perpendicular to the oblique rift zone. The ongoing evolution of the model shows that intermediate fault proportion tends to decrease with time compared to the displacement-orthogonal faults, suggesting that the far-field is more and more dominant.

6. Conclusion

The proposed stress interpretation method intuitively visualizes the surface stress field in terms of stress regime and optimal fault orientation. It allows to extract significantly more details of the model evolution than mere interpretation of strain-rate and strain fields. A comparison with analogue models and the natural Gulf of Aden shows very good agreement in many aspects. We stress that this method can be easily introduced in the post-processing step of any numerical geodynamic model.

We identify a characteristic three-phase evolution of fault patterns. Phase 1 (1-5 My): faults develop with orientations that are intermediate between the rift-direction and the displacement-orthogonal. Phase 2 (6-13 My): Rift-parallel normal faults occur at the rift flanks simultaneously with strike-slip faults and displacement-orthogonal faults in the central part of the rift system. Phase 3 (after 13 My): Displacement-orthogonal as well as intermediate orientation dominate during break-up and thereafter.

In agreement with previous studies, we correlate these steps to the following deformation processes: (i) Interaction of the far-field stress and the local stresses induced by the weakness zone generates intermediate faults. (ii) Necking-related buoyancy forces affect the local stress field and create rift-parallel faults. Additionally, strain partitioning between the rift centre and the rift flanks generates rift-parallel fault orientations at the rift borders. (iii) During break-up, far-field stress conditions become progressively important, creating intermediate and displacement-orthogonal faults.

Acknowledgments

Sascha Brune is funded by SAMPLE (South Atlantic Margin Processes and Links with onshore Evolution), Priority Program 1375 of the German Research Foundation (DFG). This study benefited greatly from discussions with Oliver Heidbach, Andrey Babeyko, and Stephan Sobolev. We thank the reviewers, Roberto Weinberg and Kenni D. Petersen for their detailed and constructive comments that greatly helped to improve this article.

References

Agostini, A., G. Corti, A. Zeoli, and G. Mulugeta (2009), Evolution, pattern and partitioning of deformation during oblique continental rifting: Inferences from lithospheric - scale centrifuge models, Geochem. Geophys. Geosyst., 10, Q11015, doi:10.1029/2009GC002676.

Agostini, A., M. Bonini, G. Corti, F. Sani, F. Mazzarini (2011), Fault architecture in the Main Ethiopian Rift and comparison with experimental models: Implications for rift evolution and Nubia-Somalia kinematics. Earth and Planetary Science Letters 301, 479-492.

Allken, V., R. S. Huismans, and C. Thieulot (2011), Three-dimensional numerical modeling of upper crustal extensional systems, J. Geophys. Res., 116, B10409, doi:10.1029/2011JB008319.

Allken, V., R. S. Huismans, and C. Thieulot (2012), Factors controlling the mode of rift interaction in brittle-ductile coupled systems: A 3D numerical study. Geochem. Geophys. Geosyst. 13(5), Q05010, doi:10.1029/2012GC004077.

Anderson, E. M. (1948), The dynamics of faulting, Oliver and Boyd, Edinburgh and London.

Artyushkov, E. V. (1973), Stresses in the Lithosphere Caused by Crustal Thickness Inhomogeneities. J J. Geophys. Res., 78, 32:7675–7708, doi:10.1029/JB078i032p07675.

Autin, J., N. Bellahsen, L. Husson, M. Beslier, S. Leroy, and E. d'Acremont (2010), Analogue models of oblique rifting in a cold lithosphere, Tectonics, 29, TC6016, doi:10.1029/2010TC002671.

Autin, J., Bellahsen, N., Leroy, S., Beslier, M.-O., d'Acremont, E., Husson, L., (this volume), Analogue models of oblique rifting: the role of structural inheritance. Tectonophysics, Special Issue: The Gulf of Aden rift.

Bassi, G. (1991), Factors controlling the style of continental rifting: insights from numerical modelling. Earth Planet. Sci. Lett., 105, 430–452.

Behn, M.D., J. Lin, and M. T. Zuber (2002), A continuum mechanics model for normal faulting using a strain-rate softening rheology: implications for thermal and rheological controls on continental and oceanic rifting, Earth Planet. Sci. Lett., 202, 725–740.

Bellahsen, N., C. Faccenna, F. Funiciello, J. Daniel, and L. Jolivet (2003), Why did Arabia separate from Africa? Insights from 3-D laboratory experiments, Earth Planet. Sci. Lett., 216, 365 – 381.

Bellahsen, N., M. Fournier, E. d'Acremont, S. Leroy, J. M. Daniel (2006), Fault reactivation and rift localization: Northeastern Gulf of Aden margin. Tectonics, 25, TC1007.

Bellahsen, N., L. Husson, J. Autin, S. Leroy, and E. d' Acremont (this volume), The effect of thermal weakening and buoyancy forces on rift localization: Field evidences from the Gulf of Aden oblique rifting, Tectonophysics, Special Issue: The Gulf of Aden rift.

Bosworth, W., P. Huchon, K. McClay (2005), The Red Sea and Gulf of Aden Basins. J. African Earth Sci., 43, 334–378.

Bott, M. H. T. (1959), The mechanics of oblique slip faulting, Geological Magazine, 96(2), 109-117

Braun, J. and C. Beaumont (1989), A physical explanation of the relation between flank uplifts and the breakup unconformity at rifted continental margins, Geology, 17, 760–764.

Brune, S., A. A. Popov, and S. V. Sobolev (2012), Modeling suggests that oblique extension facilitates rifting and continental break-up, J. Geophys. Res., 117, B08402, doi:10.1029/2011JB008860.

Brune, S., A. A. Popov, and S. V. Sobolev (2013), Quantifying the thermo-mechanical impact of plume arrival on continental break-up (in press at Tectonophysics), 10.1016/j.tecto.2013.02.009.

Buiter, S. J. H., R. S. Huismans, and C. Beaumont (2008), Dissipation analysis as a guide to mode selection during crustal extension and implications for the styles of sedimentary basins. J. Geophys. Res., 113, B06406, doi:10.1029/2007JB005272.

Burov, E. (2007), The role of gravitational instabilities, density structure and extension rate in the evolution of continental margins. In G.D. Karner, G. Manatschal, and L. M. Pinheiro (eds), Imaging, Mapping and Modelling Continental Lithosphere Extension and Breakup, Geological Society, London, Special Publications 282, 139–156.
doi:10.1144/SP282.7.

Burov, E., and S. Cloetingh (1997), Erosion and rift dynamics: new thermomechanical aspects of post-rift evolution of extensional basins. Earth Planet. Sci. Lett., 150, 7–26.

Buck, W.R. (1991), Modes of Continental Lithospheric Extension, J. Geophys. Res., 96, 20161–20178.

Clifton, A. E., R. W. Schlische, M. O. Withjack, and R. V. Ackermann (2000), Influence of rift obliquity on fault - population systematics: Results of experimental clay models, J. Struct. Geol., 22, 1491-1509, doi:10.1016/S0191-8141(00)00043-2.

Corti, G. (2004), Centrifuge modelling of the influence of crustal fabrics on the development of transfer zones: Insights into the mechanics of continental rifting architecture, Tectonophysics, 384(1 – 4), 191-208, doi:10.1016/j.tecto.2004.03.014.

Corti, G., M. Bonini, F. Innocenti, P. Manetti, and G. Mulugeta (2001), Centrifuge models simulating magma emplacement during oblique rifting, J. Geo-dyn., 31(5), 557 – 576, doi:10.1016/S0264-3707(01).

Corti, G., M. Bonini, S. Conticelli, F. Innocenti, P. Manetti, and D. Sokoutis (2003), Analogue modelling of continental extension: A review focused on the relations between the patterns of deformation and the presence of magma, Earth Sci. Rev., 63(3 – 4), 169 – 247, doi:10.1016/S0012-8252 (03)00035-7.

d'Acremont, E., S. Leroy, M.-O. Beslier, N. Bellahsen, M. Fournier, C. Robin, M. Maia, and P. Gente (2005), Structure and evolution of the eastern Gulf of Aden conjugate margins from seismic reflection data. Geophys. J. Int., 160, 869–890.

Davis, M., and N. Kusznir (2002), Are buoyancy forces important during the formation of rifted margins ? Geophys. J. Int., 149, 524–533.

Dauteuil, O., P. Huchon, F. Quemeneur, and T. Souriot (2001), Propagation of an oblique spreading center: the western Gulf of Aden, Tectonophysics, 332:423- 442.

Dick, H. J. B., J. Lin, and H. Schouten (2003), An ultraslow-spreading class of ocean ridge. Nature 426, 405–412.

Dunbar, J. A. and D. S. Sawyer (1996), Three-dimensional dynamical model of continental rift propagation and margin plateau formation. J. Geophys. Res. 101, 27845–27,863.

Ellis, A. C., H. M. Kerr, C. P. Cornwell, and D. O. Williams (1996), A tectono-stratigraphic framework for Yemen and its implications for hydrocarbon potential. Petroleum Geoscience 2, 29–42.

England, P., and D. McKenzie (1982), A thin viscous sheet model for continental deformation. Geophys. J. Royal Astr. Soc.., 70, 295–321.

Fleitout, L., and C. Froidevaux. (1982), Tectonics and Topography for a Lithosphere Containing Density Heterogeneities, Tectonics 1,1:21–56. doi:10.1029/TC001i001p00021.

Fournier, M., N. Bellahsen, O. Fabbri, and Y. Gunnell (2004), Oblique rifting and segmentation of the NE Gulf of Aden passive margin. Geochem. Geophys. Geosyst. 5.

Fournier, M., P. Huchon, K. Khanbari, and S. Leroy (2007), Segmentation and along-strike asymmetry of the passive margin in Socotra, eastern Gulf of Aden: Are they controlled by detachment faults? Geochem. Geophys. Geosyst. 8.

Gac, S., and L. Geoffroy (2009), 3D Thermo-mechanical modelling of a stretched continental lithosphere containing localized low-viscosity anomalies (the soft-point theory of plate break-up). Tectonophysics, 468 (1–4), 158–168.

Gerya, T. (2009), Introduction to Numerical Geodynamic Modelling. Cambridge University Press.

Gerya, T. (2010), Dynamical Instability Produces Transform Faults at Mid-Ocean Ridges. Science 329, 1047–1050.

Gleason, G. C., and J. Tullis (1995), A flow law for dislocation creep of quartz aggregates determined with the molten-salt cell, Tectonophysics, 247,1–23.

Granath, J. W. (2001), The Nogal Rift of northern Somalia: Gulf of Aden. Reactivation of a Mesozoic Rift. Mémoires du Muséum national d'histoire naturelle 186, 511–527.

Hébert, H., C. Deplus, P. Huchon, K. Khanbari, and L. Audin (2001), Lithospheric structure of a nascent spreading ridge inferred from gravity data : The western Gulf of Aden, J. Geophys. Res. 106, B11:26345-26363.

Hirth, G., and D. Kohlstedt (2003), Rheology of the upper mantle and the mantle wedge: A view from the experimentalists, in Inside the Subduction Factory, Geophys. Monogr. Ser., vol. 138, edited by J. Eiler, pp. 83 – 105, AGU, Washington, D. C., doi:10.1029/138GM06.

Houseman, G. and P. England (1986), Finite strain calculations of continental deformation: 1. Method and general results for convergent zones. J. Geophys. Res., 91, 3651–3663.

Huchon P, F. Jestin, J. M. Cantagrel, J. M. Gaulier, S. A. Kirbash, and A. Gafaneh A (1991), Extensional deformation in Yemen since Oligocene and the Africa – Arabia – Somalia triple junction. Annales Tectonicae. 5:141 – 163.

Huchon, P., and K. Khanbari (2003), Rotation of the syn-rift stress field of the northern Gulf of Aden margin, Yemen. Tectonophysics, 364, 147–166.

Huismans, R. S., Y. Y. Podladchikov, S. Cloetingh (2001), Transition from passive to active rifting: Relative importance of asthenospheric doming and passive extension of the lithosphere. J. Geophys. Res., 106, 11271–11291.

Huismans, R. S., and C. Beaumont (2003), Symmetric and asymmetric lithospheric extension: Relative effects of frictional-plastic and viscous strain softening, J. Geophys. Res., 108(B10), 2496, doi:10.1029/ 2002JB002026.

Huismans, R., and C. Beaumont (2011), Depth-dependent extension, two-stage breakup and cratonic underplating at rifted margins. Nature, 473, 74–78.

Kameyama, M., D. A. Yuen, S. I. Karato (1999), Thermal-mechanical effects of low-temperature plasticity (the Peierls mechanism), on the deformation of a viscoelastic shear zone. Earth Planet. Sci. Lett.,168, 159–172.

Katzman, R., U. S. ten Brink, and J. Lin (1995), Three-dimensional modeling of pull-apart basins: Implications for the tectonics of the Dead Sea Basin, J. Geophys. Res., 100, 6295–6312.

Lavier, L. L., W. R. Buck, and A. N. B. Poliakov (2000), Factors controlling normal fault offset in an ideal brittle layer. J. Geophys. Res., 105, 23431–23,442.

Lavier, L.L., and G. Manatschal (2006), A mechanism to thin the continental lithosphere at magma-poor margins, Nature, 440, 324–328.

Le Pourhiet, L., B. Huet, D. A. May, L. Labrousse, and L. Jolivet (2012), Kinematic interpretation of the 3D shapes of metamorphic core complexes, Geochem. Geophys. Geosyst., 13, Q09002, doi:10.1029/2012GC004271.

Lepvrier, C., M. Fournier, T. Bérard, and J. Roger (2002), Cenozoic extension in coastal Dhofar (southern Oman): implications on the oblique rifting of the Gulf of Aden. Tectonophysics 357, 279–293.

Leroy, S., et al. (2010), Contrasted styles of rifting in the eastern Gulf of Aden: A combined wide-angle, multichannel seismic, and heat flow survey. Geochem. Geophys. Geosyst. 11, Q07004, 1–14.

Leroy, S., et al. (2012), From rifting to oceanic spreading in the Gulf of Aden: a synthesis. Arabian J Geosci., 5, 859–901.

Mart, Y., and O. Dauteuil (2000), Analogue experiments of propagation of oblique rifts, Tectonophysics, 316, 121 – 132, doi:10.1016/S0040-1951(99), 00231-0.

McClay, K. R., and M. J. White (1995), Analogue modelling of orthogonal and oblique rifting, Mar. Pet. Geol., 12(2), 137 – 151, doi:10.1016/0264-8172(95).

Melnick, D., Y. Garcin, J. Quinteros, M. R. Strecker, D. Olago, and J. J. Tiercelin (2012), Steady rifting in northern Kenya inferred from deformed Holocene lake shorelines of the Suguta and Turkana basins. Earth Planet. Sci. Lett., 331-332, 335-346.

Montési, L. G. J., and M. D. Behn (2007), Mantle flow and melting underneath oblique and ultraslow mid-ocean ridges. Geophys. Res. Lett. 34,5.

Popov, A. A., and S. V. Sobolev (2008), SLIM3D: A tool for three-dimensional thermo mechanical modeling of lithospheric deformation with elasto-visco-plastic rheology, Phys. Earth Planet. Interiors 171, 55 – 75.

Popov, A. A., S. V. Sobolev, and M. D. Zoback (2012), Modeling evolution of the San Andreas Fault system in northern and central California. Geochem. Geophys. Geosyst. 13.

Quinteros, J., S. V. Sobolev, and A. A. Popov (2010), Viscosity in transition zone and lower mantle: Implications for slab penetration. Geophys.Res. Lett., 37, L09307.

Quinteros, J., and S. V. Sobolev (2012), Constraining kinetics of metastable olivine in the Marianas slab from seismic observations and dynamic models. Tectonophysics, 526-529, 48-55.

Quinteros, J., and S. V. Sobolev (2013), Why has the Nazca plate slowed since the Neogene?. Geology, 41, 1, 31-34.

Regenauer-Lieb, K., R. F. Weinberg, and G. Rosenbaum (2006), The effect of energy feedbacks on continental strength. Nature, 442, 67–70.

Rey, P.F. and G. Houseman (2006), Lithospheric scale gravitational flow: the impact of body forces on orogenic processes from Archaean to Phanerozoic. Geological Society, London, Special Publications 253, 153–167.

Rey, P.F., C. Teyssier, S. C. Kruckenberg, and D. L. Whitney (2011), Viscous collision in channel explains double domes in metamorphic core complexes. Geology, 39, 387–390.

Ring, U., C. Betzler, and D. Delvaux. (1992), Normal Vs. Strike-slip Faulting During Rift Development in East Africa: The Malawi Rift, Geology 20,11: 1015-1018.

Simo, J. C., and T. J. R. Hughes (2000), Computational Inelasticity, 2nd ed. Springer-Verlag, New York.

Simpson, R. W. (1997), Quantifying Anderson's fault types, J. Geophys. Res., 102(B8), 17,909-17,919.

Sokoutis, D., G. Corti, M. Bonini, J. Pierre Brun, S. Cloetingh, T. Mauduit, and P. Manetti (2007), Modelling the extension of heterogeneous hot lithosphere, Tectonophysics, 444(1 – 4), 63 – 79, doi:10.1016/j.tecto.2007.08.012.

Tamsett, D., and R. C. Searle (1988), Structure and Development of the Midocean Ridge Plate Boundary in the Gulf of Aden: Evidence from GLORIA Side Scan Sonar, J. Geophys. Res., 93,B4: 3157–3178. doi:10.1029/JB093iB04p03157.

Tommasi, A., and A. Vauchez (2001), Continental rifting parallel to ancient collisional belts: An effect of the mechanical anisotropy of the lithospheric mantle, Earth Planet. Sci. Lett., 185, 199 – 210.

Tron, V., and J. P. Brun (1991), Experiments on oblique rifting in brittle‐ductile systems, Tectonophysics, 188, 71 – 84, doi:10.1016/0040-1951(91)90315-J.

Vendeville, B., P. Cobbold, P. Davy, J. Brun, and P. Choukroune (1987), Physical models of extensional tectonics at various scales. Faulting and related processes 2, 171.

van Wijk, J. W. (2005), Role of weak zone orientation in continental lithosphere extension, Geophys. Res. Lett. 32, L02303, doi:10.1029/ 2004GL022192.

Van Wijk, J. W., and S. A. P. L. Cloetingh (2002), Basin migration caused by slow lithospheric extension. Earth Planet. Sci. Lett.,198, 275–288.

Van Wijk, J. W. and D. K. Blackman, (2005), Dynamics of continental rift propagation: the end-member modes, Earth Planet. Sci. Lett., 229, 247–258.

Watremez L, S. Leroy, S. Rouzo, E. d'Acremont, P. Unternehr, C. Ebinger, F. Lucazeau, and A. Al-Lazki (2011), The crustal structure of the north-eastern Gulf of Aden continental margin: insights from wide-angle seismic data. Geophys. J. Int., 184(2):575–594. doi:10.1111/j.1365-246X.2010.04881.x.

Wilks, K. R., and N. L. Carter (1990), Rheology of some continental lower crustal rocks, Tectonophysics, 182, 57 – 77.

Wijns, C., R. Weinberg, K. Gessner, and L. Moresi (2005), Mode of crustal extension determined by rheological layering. Earth Planet. Sci. Lett., 236, 120–134.

Withjack, M. O., and W. R. Jamison (1986), Deformation produced by oblique rifting, Tectonophysics, 126(2 – 4), 99 – 124, doi:10.1016/0040-1951(86), 90222-2.

Ziegler, P. A., and S. Cloetingh (2004), Dynamic processes controlling evolution of rifted basins, Earth Sci. Rev., 64, 1 – 50.

Zuber, M. T. and E. M. Parmentier (1986), Lithospheric necking: a dynamic model for rift morphology. Earth Planet. Sci. Lett., 77, 373–383.